Prototype pre-clinical PET scanner with depth-of-interaction measurements using single-layer crystal array and single-ended readout

2017 Phys. Med. Biol. 62 3983

(http://iopscience.iop.org/0031-9155/62/10/3983)

IOP Publishing | Institute of Physics and Engineering in Medicine Physics in Medicine & Biology

Phys. Med. Biol. **62** (2017) 3983–3996 https://doi.org/10.1088/1361-6560/aa64c7

Prototype pre-clinical PET scanner with depth-of-interaction measurements using single-layer crystal array and single-ended readout

Min Sun Lee[1,2], Kyeong Yun Kim[1,3], Guen Bae Ko[1,3] and Jae Sung Lee[1,3,4]

[1] Department of Nuclear Medicine, College of Medicine, Seoul National University, Seoul, Republic of Korea
[2] Interdisciplinary Program in Radiation Applied Life Science, Seoul National University, Seoul, Republic of Korea
[3] Department of Biomedical Sciences, College of Medicine, Seoul National University, Seoul, Republic of Korea

E-mail: jaes@snu.ac.kr

Received 6 December 2016, revised 30 January 2017
Accepted for publication 6 March 2017
Published 13 April 2017

Abstract

In this study, we developed a proof-of-concept prototype PET system using a pair of depth-of-interaction (DOI) PET detectors based on the proposed DOI-encoding method and digital silicon photomultiplier (dSiPM). Our novel cost-effective DOI measurement method is based on a triangular-shaped reflector that requires only a single-layer pixelated crystal and single-ended signal readout. The DOI detector consisted of an 18 × 18 array of unpolished LYSO crystal (1.47 × 1.47 × 15 mm^3) wrapped with triangular-shaped reflectors. The DOI information was encoded by depth-dependent light distribution tailored by the reflector geometry and DOI correction was performed using four-step depth calibration data and maximum-likelihood (ML) estimation. The detector pair and the object were placed on two motorized rotation stages to demonstrate 12-block ring PET geometry with 11.15 cm diameter. Spatial resolution was measured and phantom and animal imaging studies were performed to investigate imaging performance. All images were reconstructed with and without the DOI correction to examine the impact of our DOI measurement. The pair of dSiPM-based DOI PET detectors showed good physical performances respectively: 2.82 and 3.09 peak-to-valley ratios, 14.30% and 18.95% energy resolution, and 4.28 and

[4] Author to whom any correspondence should be addressed.

4.24 mm DOI resolution averaged over all crystals and all depths. A sub-millimeter spatial resolution was achieved at the center of the field of view (FOV). After applying ML-based DOI correction, maximum 36.92% improvement was achieved in the radial spatial resolution and a uniform resolution was observed within 5 cm of transverse PET FOV. We successfully acquired phantom and animal images with improved spatial resolution and contrast by using the DOI measurement. The proposed DOI-encoding method was successfully demonstrated in the system level and exhibited good performance, showing its feasibility for animal PET applications with high spatial resolution and sensitivity.

Keywords: depth of interaction, PET, animal PET, silicon photomultiplier

(Some figures may appear in colour only in the online journal)

1. Introduction

Preclinical or animal imaging, is widely conducted in biomedical research for the evaluation of new drugs, imaging probes, and diseases models. Positron emission tomography (PET) is one of the widely used imaging techniques in preclinical research and provides functional information at the molecular level (Wienhard *et al* 1994, Cherry *et al* 1997, Chatziioannou *et al* 1999, Phelps 2000, Surti *et al* 2005, Huisman *et al* 2007, Lee 2015). Small-animal-dedicated PET systems require high and uniform spatial resolution to assess small lesions and high sensitivity to acquire images with smaller voxels with high signal-to-noise ratio (SNR) (Pomper and Lee 2005). However, since these two factors compromise each other, to achieve both high spatial resolution and sensitivity remains a challenge. Numerous approaches have been proposed to solve this issue (Qi *et al* 1998, Levin and Hoffman 1999, Stickel *et al* 2007); among these, the depth-of-interaction (DOI) information is one of the key solutions to achieve fine resolution and high sensitivity simultaneously (MacDonald and Dahlbom 1998, Ito *et al* 2011).

Various methods have been proposed for development of PET detectors with DOI-encoding capability. Some DOI-encoding designs utilize multi-layer scintillation crystal arrays (Saoudi *et al* 1999, Inadama *et al* 2006) or employ two or more photosensors and readout channels (Yang *et al* 2006, Yamaya *et al* 2011). These approaches yield good DOI resolution and have exhibited good imaging performance in the system level (Wang *et al* 2006, Yamaya *et al* 2006, Yang *et al* 2008); however, they require high manufacturing costs or sophisticated construction methods. Therefore, the development of simple and cost-efficient DOI-encoding techniques using a single-layer of crystal array and single-ended readout has been attempted by several groups, including ours. One approach for the development of low-cost DOI detectors is controlling light distribution or output pulse shape in pixelated crystals (Du *et al* 2009, Miyaoka *et al* 2009, Ito *et al* 2010, Son *et al* 2017). Another approach is using a monolithic crystal from which DOI information is extracted by measuring the extent of the light distribution (van Dam *et al* 2011). However, not many of these low-cost DOI measurement approaches have been investigated in terms of their impact on imaging performance of the system.

Our group has previously devised a method based on the light dispersion in a crystal array to decode DOI information in a mono-layer pixelated scintillation crystal using a single-ended readout (Ito *et al* 2010). Light dispersion was achieved by wrapping the crystal array with

triangular teeth-shaped reflectors that were crossed over to each other. Owing to the reflector configuration, the amount and direction of light dispersion depends on the DOI; hence, DOI information is encoded in the detector response. A digital silicon photomultiplier (dSiPM) was used as the photosensor in this study as the SiPM is now widely accepted in PET systems (Kwon *et al* 2011, Yamaya *et al* 2011, Yoon *et al* 2012, Marcinkowski *et al* 2016, Ko *et al* 2016b). The dSiPM is beneficial for implementing our continuous DOI-encoding method because energy information generated from each pixel of the dSiPM array is digitally recorded and thus available for the easy and flexible estimation of light distribution (Lee and Lee 2015).

We have shown the feasibility of our DOI PET detector design and explored its characteristics based on Monte Carlo simulation studies (Ito *et al* 2010). Additionally, we have experimentally evaluated the performance of our DOI detectors based on both photomultiplier tube (PMT) and dSiPM and obtained promising physical performances regarding high resolution and sensitivity (Ito *et al* 2013, Lee and Lee 2015). In this study, we developed a prototype PET system by rotating a pair of dSiPM-based DOI detectors, one detector rotating while the other one stationary, for the proof-of-concept evaluation of the proposed DOI-encoding method in the system level and showed its feasibility through phantom and small-animal experiments.

2. Materials and methods

2.1. DOI-encoding PET detector module

To encode DOI information in a continuous single-layer crystal array with single-ended readout, our group has proposed a simple and cost-effective method in which the reflectors have the shape of triangular teeth that are perpendicularly crossed over each other (figure 1). Because a teeth-shaped reflector partially covers each crystal, optical photons can disperse through the crystal array. Moreover, because reflectors are configured in opposite directions along the *x*- and *y*-directions, the amount and direction of light dispersion shows different patterns depending on the three-dimensional (3D) interaction positions of gamma ray. Consequently, DOI information is encoded through different light dispersion patterns along the *x*- and *y*-directions that are recorded as detector responses with its own statistical characteristics. The continuous DOI detector developed in this study is hereafter referred to as cDOI detector.

For each cDOI detector, a digital SiPM (DPC-3200-22-44, Philips Digital Photon Counting) was optically coupled with an 18 × 18 array of unpolished LYSO crystal (Crystal Photonics Inc., FL, US). The detector specifications are described in table 1. The crystals were wrapped with a triangular teeth-shaped enhanced specular reflector polymer (3M, St. Paul, MN, USA) as shown in figure 1. A 1 mm-thick light guide was inserted between crystal array and dSiPM for efficient light sharing and a window-shaped reflector was used to reduce the light loss due to dead spaces between dSiPM pixels. All components were optically coupled with optical grease (BC-630; Saint-Gobain, Paris, France).

2.2. Prototype PET scanner

A pair of cDOI detectors was used in this study to demonstrate a 12-block ring PET system with a diameter of 11.15 cm with specifications described in table 2. One cDOI detector was fixed on the base plate, while the other one and the object were rotated on two motorized rotation stages (Namil Optical Instruments Co., Incheon, Korea), as shown in figure 2. The detector on stage 1 rotated with a 30° step to form every possible detector configuration and the object on stage 2 rotated with a 30° step over the imaging FOV to cover all possible line-of-responses (LORs) for the proper image reconstruction.

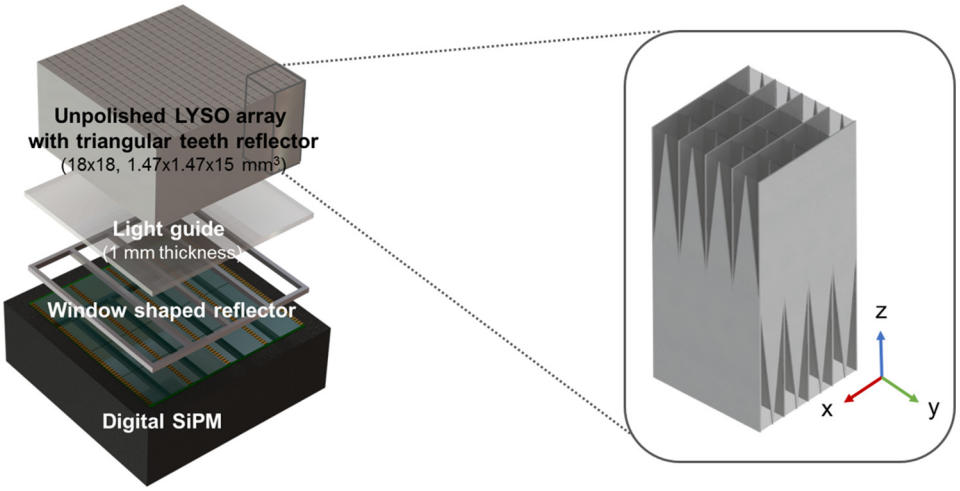

Figure 1. Design and components of the cDOI PET detector.

Table 1. Specifications of cDOI PET detector.

Scintillation crystal	
Scintillation material	LYSO
Size (mm^3)	$1.47 \times 1.47 \times 15$
Pitch (mm)	1.57
Array size	18×18
Digital SiPM (DPC-3200-22-44)	
Pixel size (mm^2)	3.2×3.8775
No. of SPADs/pixel[a]	3200
No. of pixels/sensor	64 (8×8)
PDE (%)[b]	40

[a] SPAD: Single photon avalanche diodes.
[b] PDE: Photon detection efficiency.

The dSiPM sensor offers a configurable trigger and validation logic and data acquisition protocol (Frach *et al* 2009, Marcinkowski *et al* 2016), and we previously evaluated and optimized the sensor configuration to acquire good detector performances (Lee and Lee 2015). In this study, we used the following sensor configurations of dSiPM: trigger scheme 2, validation scheme 4, validation length of 40 ns, integration length of 165 ns, coincidence time window of 40 ns, full-tile neighbor logic, and inhibition of the 10% of cells with the highest dark count. Data acquisition was managed by a Philips Digital Photon Counting Technology Evaluation Kit (PDPC-TEK) connected to a PC. As shown in figure 2, experimental setup was placed inside a temperature control box (CT-BDI150; Coretech Inc., Korea) set to 0 °C for constant temperature and dark count noise suppression.

2.3. DOI positioning scheme

For the depth calibration, we conducted coincidence measurements for each detector and obtained their DOI responses at four different depth positions, and 0.7 MBq ^{22}Na point source

Table 2. Specifications of prototype cDOI PET system.

Parameter	Value
Face-to-face distance between detectors (cm)	11.15
No. of crystal rings	18
No. of crystals/ring[a]	216
Total no. of crystals[b]	3888
Axial FOV (cm)	2.83

[a] No. of crystal/ring: number of crystals in one ring.
[b] Total no. of crystals: total number of crystals in the prototype system.

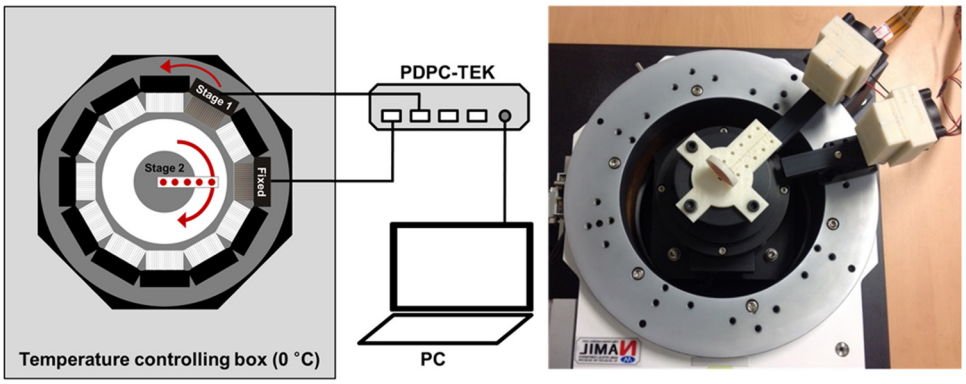

Figure 2. Prototype cDOI PET scanner consisting of two cDOI PET detector modules placed on two motorized rotation stages.

(Eckert & Ziegler, Valencia, CA, USA) was used here. A slab crystal with dimensions of $28 \times 20 \times 0.75\,\text{mm}^3$ was used for electronic collimation and provided a 0.75 mm-wide beam to selectively irradiate four depths of the crystal block at 1.875, 5.625, 9.375, and 13.125 mm from the dSiPM (figure 3(a)).

The cDOI detector showed 3D-position-dependent detector responses with characteristic mean and standard deviation values (Lee and Lee 2015). The position information was obtained using a maximum-likelihood estimation (MLE) with a statistically modeled detector response, as shown in the equation below (Ling *et al* 2007, Lee and Lee 2015).

$$L(\vec{x}|S) = \prod_{i=1}^{64} \frac{1}{\sigma_i(\vec{x})\sqrt{2\pi}} \exp\left(-\frac{(s_i - \mu_i(\vec{x}))^2}{2\sigma_i^2(\vec{x})}\right)$$

$$\hat{\vec{x}}_{\text{ML}} = \arg \max_{\forall \vec{x}} L(\vec{x}|S)$$

Each 8×8 detector response was modeled as an independent Gaussian distribution (Ling *et al* 2007). The likelihood function $L(\vec{x}|S)$ of a detector signal S (s_1, …, s_{64}) of a single event at each 3D position $\vec{x}$ was composed of the product of independent Gaussian functions at the ith channel. We denote $\mu_i(\vec{x})$ and $\sigma_i(\vec{x})$ as the mean and standard deviation at ith channel, which are functions of the 3D position $\vec{x}$. Two look-up tables consisting of the means and standard deviations of the detector responses were generated for training data using 70%

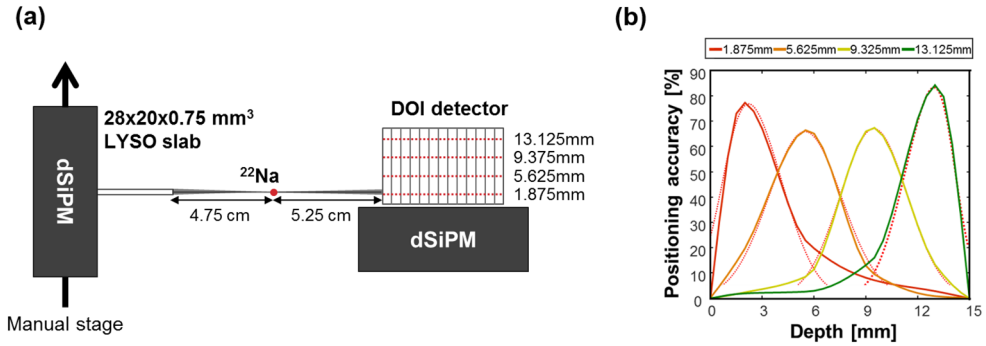

Figure 3. (a) Experimental setup of depth calibration. (b) Conversion of DOI positioning accuracy into DOI resolution.

of depth calibration data for each 3D interaction position. The remaining 30% were used to test the likelihood function. Finally, maximum likelihood (ML) estimate ($\hat{\vec{x}}_{\mathrm{ML}}$), which is the estimated interaction position, was obtained by maximizing the likelihood function $L(\vec{x}|S)$.

2.4. Detector-level performance evaluation

2.4.1. Evaluation on crystal surface treatment. Because our DOI-encoding design is based on light sharing among crystals, the crystal surface treatment conditions play an important role in controlling light dispersion. Therefore, appropriate surface conditions are required that provide good DOI performance without detector performance degradation. Here, we tested two types of unpolished LYSO crystal blocks with different surface roughness, which was controlled by lapping the crystal surface with two abrasive grit sizes:

(1) 200 grit for a rougher surface,
(2) 1200 grit for a finer surface.

Four sides of the crystal surface were unpolished by treating with abrasive grits, while the upper and lower side of crystal surfaces were polished. It must be noted that experimental conditions and DOI positioning scheme were not fully optimized at this stage since this crystal surface treatment experiment was conducted in the past. In this study, the depth calibration was performed at 3, 6, 9, and 12 mm of the crystal block to evaluate depth-dependent detector performances. Flood histogram quality, energy resolution, and DOI positioning accuracy were evaluated to determine the appropriate surface treatment conditions.

2.4.2. Performance evaluation of DOI PET detectors. To assess performances of cDOI detectors, the peak-to-valley ratio of flood histogram, energy resolution, and DOI resolution were evaluated and reported here. Flood histograms were generated by plotting two-dimensional (2D) histograms of gamma ray interaction positions obtained by weighted means of 64 pixel values. The peak-to-valley ratio was evaluated to assess flood histograms quality. Energy spectra were generated by summing 64 pixel values and energy resolutions were reported by measuring full-width-at-half-maximum (FWHM) of each spectrum.

To quantify DOI-decoding performance, we measured the estimation accuracy of the gamma ray interaction position in the crystal array (positioning accuracy). The positioning accuracy was calculated using depth calibration data, which corresponded to the percentage

ratio of obtained MLE-based position estimates at each known position. Two different strategies for DOI estimation were compared:

(1) Method 1: simultaneous MLE of the crystal position (x, y) and depth (z),
(2) Method 2: estimation based on the 2D center of mass (flood histogram) of the crystal position (x, y) and 1D MLE of the depth (z), which were used in our previous study (Lee and Lee 2015).

Finally, DOI resolution was reported by converting the positioning accuracies of Method 1 (3D estimation) into millimeters. Based on discrete positioning accuracies, positioning accuracy profiles along depths were generated by piecewise cubic interpolation (figure 3(b)). The depth profile generated was fitted with Gaussian distribution and DOI resolutions were calculated in FWHM values. All detector performances reported were averaged over four depths and all 324 crystals.

2.5. System-level performance evaluation

2.5.1. Spatial resolution measurement. Spatial resolution of the prototype system was measured using a 0.7 MBq ^{22}Na point source embedded in a 1 cm^3 acrylic cube. The measurement was conducted at the axial center of the FOV at 0, 5, 10, 15, 25, and 30 mm from the center. MLE-based DOI correction was applied and data were converted into the list-mode data using a custom-built software tool (Ko *et al* 2016a) with an energy window of 350–650 keV. No normalization, random, attenuation, and scatter correction was applied. The 3D list-mode ordered-subset estimation maximization (OSEM) was used for image reconstruction with and without DOI information. For DOI reconstruction, we did not include any of point spread function modeling. No Gaussian filter was applied to the reconstructed images. Spatial resolution of the prototype system was reported with FWHM and full-width-at-tenth-maximum (FWTM) values of the radial and tangential profiles.

2.5.2. Phantom and animal imaging studies. Phantom study was performed using a hot-rod phantom with various diameters of 1.0, 1.1, 1.2, 1.3, 1.4, and 1.5 mm. Phantom was filled with 55.5 MBq of ^{64}Cu ($T_{1/2} = 12.701$ h) and was placed at the center and at 1.5 cm from the center to examine the impact of DOI correction capability on the imaging performance. Imaging data were acquired for 1 h using our prototype system.

The animal study was approved by Institutional Animal Care and Use Committee of Seoul National University. Two eight-week-old BALB/c mice (25 g and 27 g) were anesthetized by continuous administration of isoflurane mixed with oxygen. ^{18}F-FDG with 45 MBq activity was injected to each mouse through the tail vein. After 30 min uptake time, a 12 min PET data set was acquired using the prototype system. An x-ray computed tomography image was acquired before the PET scan using a GE eXplore VISTA PET/CT scanner for spatial registration.

For normalization correction, a 2.96 MBq ^{68}Ge annulus source (PET-7.3A5.8; Sanders Medical Products Inc., TN, USA) that covered the entire FOV was used and data were acquired for 7 h for direct normalization. No random, attenuation, and scatter correction was applied. The phantom and animal data were reconstructed with 3D list-mode OSEM with and without DOI information. An isotropic Gaussian filter with a 0.8 mm FWHM was applied to the reconstructed images. In the case of the hot-rod phantom, 12 axial slices were summed to acquire sufficient counts.

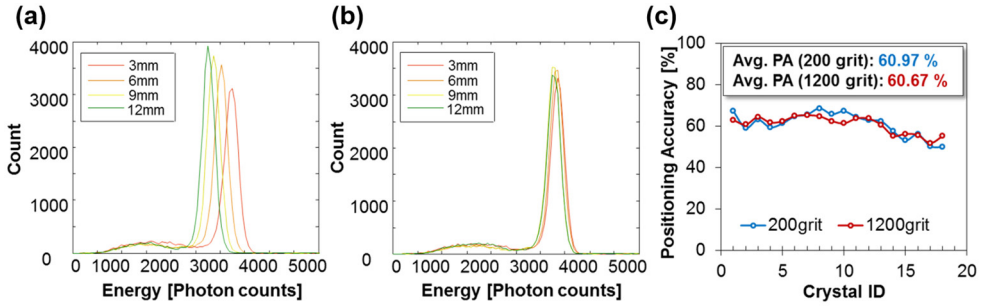

Figure 4. Effect of crystal surface treatment on cDOI detector. Energy spectra at the center crystal in the 18 × 18 crystal array acquired from (a) the 200-grit crystal and (b) the 1200-grit crystal. (c) DOI positioning accuracies for 200-grit and 1200-grit crystals for 18 crystals at the center row.

3. Results

3.1. Evaluation of crystal surface treatment

The energy resolution of cDOI detector at the center crystal of the crystal array, which was averaged over all depths, was 10.78% for the 200-grit and 9.72% for the 1200-grit crystal array. The DOI-dependent shift of the primary peak position in energy spectra was less severe in the 1200-grit crystal array (figures 4(a) and (b)). The average DOI positioning accuracy at the center crystal ((9, 8) position in the flood histogram) obtained by MLE was 68.55% and 64.71% for the 200- and 1200-grit crystal array, respectively. The DOI performance was fairly uniform for 18 crystals at the center row (9th row) of crystal array and the average DOI positioning accuracy was 60.97% and 60.67% for the 200- and 1200-grit crystal arrays, respectively, as shown in figure 4(c).

We note that the positioning accuracy acquired in the surface treatment study was worse than that of the prototype detectors due to the different depth calibration setup. The interval in depth calibration (3 mm) was shorter than that of the prototype system (3.75 mm), which increased uncertainties in positioning. However, this discrepancy in experimental setup have no significant effect on this comparison study. The quality of two flood histograms was almost equivalent. Accordingly, we decided to use 1200-grit-lapped unpolished crystals for the prototype system.

3.2. Performance of DOI PET detectors

The performances of two cDOI PET detectors are summarized in table 3 in terms of peak-to-valley ratio which represents the flood histogram quality, energy resolution, and MLE-based positioning accuracies. In this table, DOI positioning accuracies obtained using the two DOI estimation methods (simultaneous and sequential estimations of crystal position and depth) were compared for all 324 crystals and only for crystals at the left and right edges. Figure 5 shows the flood histogram and 2D map of the positioning accuracies for two DOI estimation methods, which is averaged over four depths.

As shown in figure 5(a), cDOI detectors showed good and easy crystal identification except for the crystals at the left and right edges. The blurring of the edge crystals is due to our reflector configuration: crystal positions shift toward the center when events occur far from the detector. We solved this issue by applying MLE-based positioning, which estimates the crystal and depth position simultaneously. By applying the simultaneous crystal and depth

Table 3. cDOI PET detector performances averaged over all 324 crystals.

Parameter			Block 1	Block 2
Peak-to-valley ratio			2.82	3.09
Energy resolution (%)			14.30 ± 1.43	18.95 ± 2.93
DOI positioning accuracy (%)	Method 1[a]	All	71.80 ± 4.33	72.31 ± 4.48
		Edges	73.63 ± 6.40	75.26 ± 5.73
	Method 2[b]	All	71.26 ± 4.25	71.56 ± 4.28
		Edges	68.98 ± 6.01	69.60 ± 5.75
DOI resolution (mm)			4.28 ± 0.32 (minimum: 3.53, maximum: 5.54)	4.24 ± 0.28 (minimum: 3.40, maximum: 5.06)

[a] Method 1: Simultaneous estimation of crystal position and depth.
[b] Method 2: Estimation of only depth after identifying crystal position on flood histogram.

position estimation, described as Method 1 in table 3, we obtained a higher positioning accuracy than Method 2, especially at the edge crystals. This improvement is more clearly seen in figures 5(b) and (c). The cDOI detectors showed a reasonably good energy resolution. Block 2 shows worse energy resolution compared to Block 1 because of oxidization and color change of epoxy glue that was used for assembling crystal block. The color change in adhesive material leaded to energy performance degradation, and the color change was more severe in Block 2 which was purchased earlier in time. By using MLE-based positioning method, interaction positions were successfully estimated for the 324 crystals and four depth positions, as described in table 3 (71.80 % and 72.31 % accuracy). By converting the positioning accuracy, we obtained the corresponding DOI resolutions expressed in millimeters, 4.28 mm and 4.24 mm in average for each detector, while the best DOI resolution was 3.53 mm and 3.40 mm, respectively.

3.3. Spatial resolution of prototype system

We measured system spatial resolution to investigate how it is influenced by DOI correction. The spatial resolutions in the radial and tangential directions with and without DOI correction were reported in FWHM values, as summarized in table 4. Figures 6(a) and (b) shows the radial and tangential resolutions with and without DOI correction in FWHM and FWTM values. In our prototype system, a sub-millimeter spatial resolution was achievable at the center of the FOV. By applying MLE-based DOI correction with an accuracy of 71.80% and 72.31%, the radial spatial resolution improved, especially in the peripheral regions (maximum 36.92% improvement). Moreover, as shown in figure 6(a), a uniform spatial resolution of less than 1.2 mm was achievable within 5 cm in transverse PET FOV. In addition to the resolution in the radial direction, the tangential resolution was also improved after DOI correction was applied.

3.4. Phantom and animal imaging studies

Figure 7 shows the reconstruction image of the hot-rod phantom acquired without and with DOI correction (a) at the center of the FOV and (b) at 1.5 cm from the center of the FOV. In both cases, the image resolution and resolution uniformity along the FOV improved after applying DOI correction and no significant artifacts were observed. In figure 7(a), a hot rod with size of 1.2 mm is clearly resolvable after DOI correction and even a 1.1 mm-rod is distinguishable. Additionally, the phantom image acquired at the off-center position (figure 7(b))

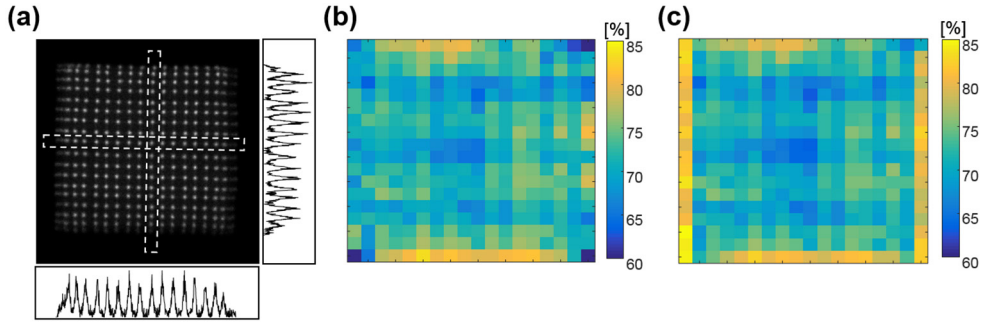

Figure 5. Performance of representative cDOI PET detector. (a) Flood histogram, (b) 2D map of the MLE-based DOI positioning accuracies obtained using only depth position estimation (Method 2), and (c) 2D map of the MLE-based DOI positioning accuracies determined using simultaneous crystal and depth position estimation (Method 1).

Table 4. Spatial resolution expressed in FWHM.

Radial position (mm)	With DOI		Without DOI		Improvement (%)	
	Radial	Tangential	Radial	Tangential	Radial	Tangential
0	0.94	1.05	0.92	1.02	−3.13	−2.62
5	1.00	1.03	1.02	1.15	1.41	10.31
10	0.99	1.16	1.17	1.18	15.11	1.26
15	1.10	1.17	1.28	1.21	14.07	3.96
25	1.21	1.20	1.60	1.45	23.99	17.32
30	1.47	1.28	2.32	1.65	36.92	22.50

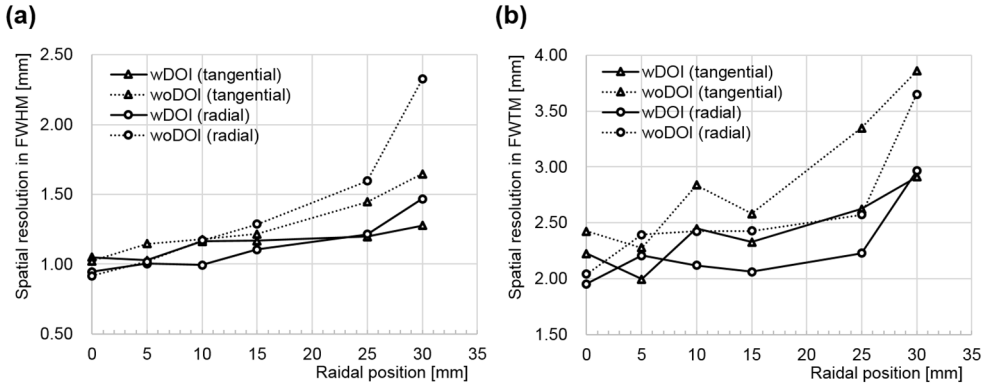

Figure 6. Spatial resolution of the prototype cDOI PET system measured using a ^{22}Na point source along the radial position; is reported in (a) FWHM and (b) FWTM.

demonstrates that our prototype system provides better spatial resolution over the entire imaging FOV than the system without DOI measurement.

Figure 8 shows reconstruction images of mice acquired (a) without DOI correction, and (b) with DOI correction. By using our prototype system, the myocardial uptake was clearly seen in the mouse after DOI correction. Although our system was demonstrated by just two

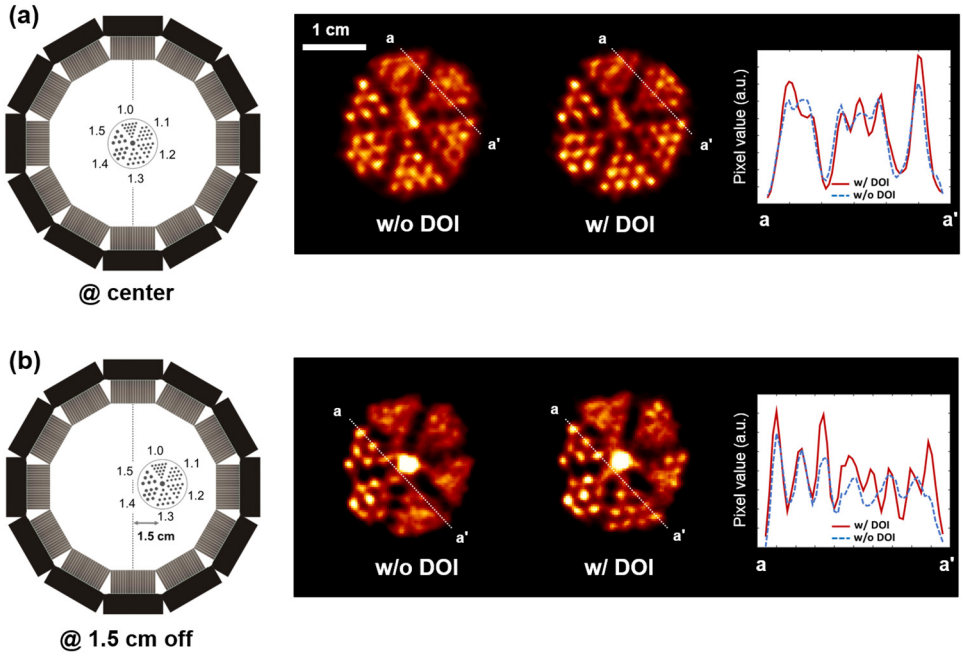

Figure 7. Hot-rod phantom images acquired using the prototype cDOI PET system. The hot-rod phantom was filled with ^{64}Cu and data were acquired for 60 min. Images obtained without and with the DOI correction (a) at the center of the FOV and (b) at 1.5 cm from the center of the FOV.

detector modules, which is not easy to acquire sufficient counts, DOI correction using our DOI-encoding method was revealed to be effective.

4. Discussion

In this study, we developed an animal-dedicated proof-of-concept DOI PET system using a pair of detectors. First, we conducted an experimental evaluation to determine the appropriate surface conditions of scintillation crystal elements. Because our DOI-encoding method is based on the light dispersion across the crystal array, we expected better DOI performance for rougher crystal surface that allows relatively broader light dispersion. However, unpolished crystals with different surface conditions did not show significant differences in detector performance. However, the rougher surface yielded DOI-dependent shift in the energy spectrum peak, indicating light loss in the upper crystal block and leading to energy spectrum blurring and system performance degradation (figure 4(a)). Accordingly, we selected the unpolished crystals with finer surface treatment for the cDOI detector development.

The DOI detector pair showed good intrinsic performance except for crystal blurring at the edges of flood histogram. Using the conventional crystal clustering method, which is based on the flood histogram generated by a center-of-mass calculation, the merged crystals at the edges could not be well discriminated, providing wrong crystal and depth information (figures 5(a) and (b)). Depth-dependent flood histogram generation is a possible solution for more accurate crystal identification (Ito *et al* 2013). MLE-based positioning method, which estimates the crystal and depth position simultaneously, is another approach for the classification of the

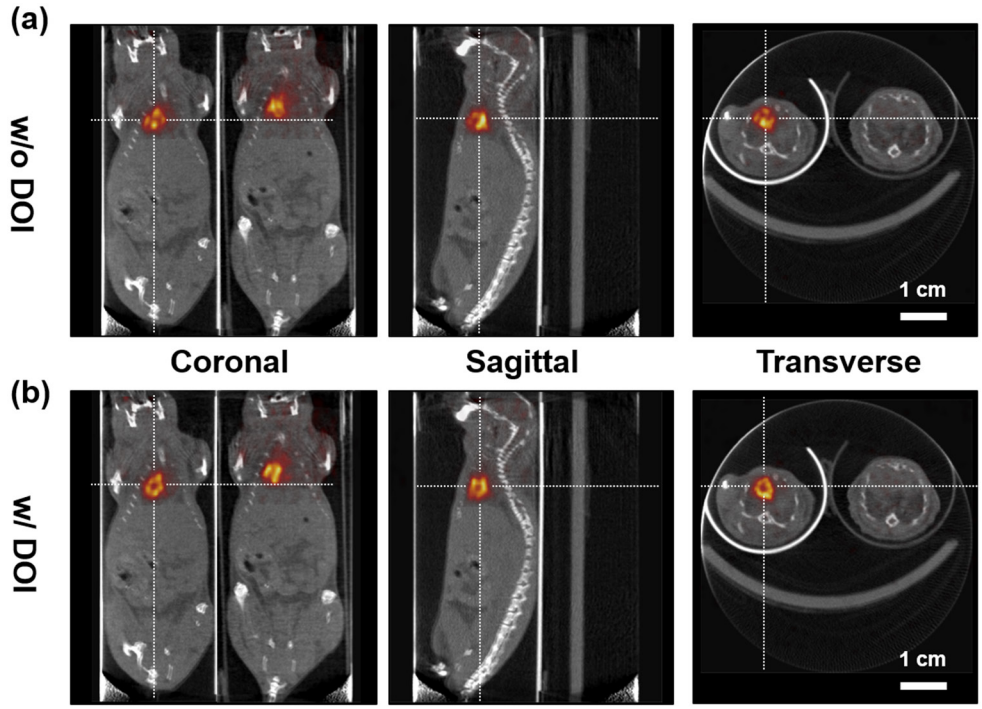

Figure 8. PET/CT images of BALB/c mice acquired after injection of ^{18}F-FDG acquired for 12 min. Images obtained (a) without the DOI correction and (b) with the DOI correction.

merged crystals. By comparing the positioning accuracies in the merged crystals at the edges, as reported in table 3, MLE-based 3D positioning technique was determined to be successful.

Regarding positioning accuracies shown in table 3, the simultaneous 3D position estimation exhibited higher positioning accuracy than the sequential estimation. Based on 3D MLE positioning, we obtained an average DOI resolution of approximately 4 mm, which enables a four-step DOI correction in a 15 mm-long crystal. A slightly worse positioning accuracy was observed in the gaps between sensor pixels, as shown in figure 5(c), although a window-shaped reflector was used to reduce the light loss. MLE-based positioning demands a relatively long computation time and large memory consumption. If this algorithm is applied to the next-generation full-ring system, a hardware/firmware implementation of this algorithm will be necessary for real-time position estimation.

Based on the four-step DOI correction, we observed considerable improvements in spatial resolution and resolution uniformity, especially at the peripheral FOV. A sub-millimeter spatial resolution was observed within 2 cm and a uniform resolution was achieved within the 5 cm in transverse PET FOV after DOI correction. The impact of DOI correction was also obvious in phantom and animal imaging studies. After DOI correction, the resolution uniformity increased and hot lesions with size up to 1.1 mm were well resolved. We expect to obtain better image resolution and contrast with additional scattering, attenuation, and random error corrections.

Several limitations exist in the demonstration of a ring-like PET system using a pair of detectors. Because we used two motorized rotation stages, artifacts might arise from detector misalignment and center-of-rotation errors. The impact of detector misalignment is greater

in a two-detector system than a full-ring system because it can cause LOR mis-positioning at every angle. These systematic errors might lead to degradation of spatial resolution and image contrast. In addition, the acquisition of a sufficiently large number of counts is difficult in PET studies using short-half-life radioisotopes (e.g. ^{18}F with 2 h) and PET detector pair. Therefore, we expect to obtain better image quality in our next-generation full-ring system.

5. Summary and conclusion

In this study, we developed a prototype PET system with a DOI-encoding scheme that is cost-effective, allows easy crystal identification, and yields good energy and DOI resolutions. The PET system has excellent spatial resolution and resolution uniformity, indicating that a future full-ring PET system based on this technology will be well suited for scanning small animals. Moreover, because our prototype system is based on silicon photomultipliers, this technology will be also useful for the development of next-generation PET/MRI systems.

Acknowledgments

We thank Juri Na for assistance with animal preparation and handling. This work was supported by grants from National Research Foundation of Korea (NRF) funded by the Korean Ministry of Science, ICT and Future Planning (grant no. NRF-2014M3C7034000 and NRF-2016R1A2B3014645).

References

Chatziioannou A F, Cherry S R, Shao Y P, Silverman R W, Meadors K, Farquhar T H, Pedarsani M and Phelps M E 1999 Performance evaluation of microPET: a high-resolution lutetium oxyorthosilicate PET scanner for animal imaging *J. Nucl. Med.* **40** 1164–75

Cherry S R *et al* 1997 MicroPET: a high resolution PET scanner for imaging small animals *IEEE Trans. Nucl. Sci.* **44** 1161–6

Du H, Yang Y, Glodo J, Wu Y, Shah K and Cherry S R 2009 Continuous depth-of-interaction encoding using phosphor-coated scintillators *Phys. Med. Biol.* **54** 1757–71

Frach T, Prescher G, Degenhardt C, de Gruyter R, Schmitz A and Ballizany R 2009 The digital silicon photomultiplier—principle of operation and intrinsic detector performance *IEEE Nuclear Science Symp. Conf. Record* pp 1959–65

Huisman M C, Reder S, Weber A W, Ziegler S I and Schwaiger M 2007 Performance evaluation of the Philips MOSAIC small animal PET scanner *Eur. J. Nucl. Med. Mol. Imaging* **34** 532–40

Inadama N, Murayama H, Yamaya T, Kitamura K, Yamashita T, Kawai H, Tsuda T, Sato M, Ono Y and Hamamoto M 2006 Preliminary evaluation of four-layer BGO DOI-detector for PET *IEEE Trans. Nucl. Sci.* **53** 30–4

Ito M, Hong S J and Lee J S 2011 Positron emission tomography (PET) detectors with depth-of-interaction (DOI) capability *Biomed. Eng. Lett.* **1** 70–81

Ito M, Lee J S, Park M J, Sim K S and Hong S J 2010 Design and simulation of a novel method for determining depth-of-interaction in a PET scintillation crystal array using a single-ended readout by a multi-anode PMT *Phys. Med. Biol.* **55** 3827–41

Ito M, Lee M S and Lee J S 2013 Continuous depth-of-interaction measurement in a single-layer pixelated crystal array using a single-ended readout *Phys. Med. Biol.* **58** 1269–82

Ko G B *et al* 2016b Simultaneous multi-parametric PET/MRI with silicon photomultiplier PET and ultra-high field MRI for small animal imaging *J. Nucl. Med.* **57** 1309–15

Ko G B, Kim K Y, Yoon H S, Lee M S, Son J-W, Im H-J and Lee J S 2016a Evaluation of a silicon photomultiplier PET insert for simultaneous PET and MR imaging *Med. Phys.* **43** 72–83

Kwon S I *et al* 2011 Development of small-animal PET prototype using silicon photomultiplier (SiPM): initial results of phantom and animal imaging studies *J. Nucl. Med.* **52** 572–80

Lee J S 2015 Innovative physics and engineering research in nuclear medicine and molecular imaging: a message from the Associate Editor *Nucl. Med. Mol. Imaging* **49** 249–50
Lee M S and Lee J S 2015 Depth-of-interaction measurement in a single-layer crystal array with a single-ended readout using digital silicon photomultiplier *Phys. Med. Biol.* **60** 6495–514
Levin C S and Hoffman E J 1999 Calculation of positron range and its effect on the fundamental limit of positron emission tomography system spatial resolution *Phys. Med. Biol.* **44** 781–99
Ling T, Lewellen T K and Miyaoka R S 2007 Depth of interaction decoding of a continuous crystal detector module *Phys. Med. Biol.* **52** 2213–28
MacDonald L R and Dahlbom M 1998 Parallax correction in PET using depth of interaction information *IEEE Trans. Nucl. Sci.* **45** 2232–7
Marcinkowski R, Mollet P, Van Holen R and Vandenberghe S 2016 Sub-millimetre DOI detector based on monolithic LYSO and digital SiPM for a dedicated small-animal PET system *Phys. Med. Biol.* **61** 2196–212
Miyaoka R S, Li X, Lockhart C and Lewellen T K 2009 New continuous miniature crystal element (cMiCE) detector geometries *IEEE Nuclear Science Symp. Conf. Record* pp 3639–42
Phelps M E 2000 Positron emission tomography provides molecular imaging of biological processes *Proc. Natl Acad. Sci. USA* **97** 9226–33
Pomper M G and Lee J S 2005 Small animal imaging in drug development *Curr. Pharm. Des.* **11** 3247–72
Qi J, Leahy R M, Cherry S R, Chatziioannou A and Farquhar T H 1998 High-resolution 3D Bayesian image reconstruction using the microPET small-animal scanner *Phys. Med. Biol.* **43** 1001–13
Saoudi A, Pepin C M, Dion F, Bentourkia M, Lecomte R, Andreacoet M, Casey M, Nutt R and Dautet H 1999 Investigation of depth-of-interaction by pulse shape discrimination in multicrystal detectors read out by avalanche photodiodes *IEEE Trans. Nucl. Sci.* **46** 462–67
Son J W, Lee M S and Lee J S 2017 A depth-of-interaction PET detector using a stair-shaped reflector arrangement and a single-ended scintillation light readout *Phys. Med. Biol.* **62** 465–83
Stickel J R, Qi J and Cherry S R 2007 Fabrication and characterization of a 0.5 mm lutetium oxyorthosilicate detector array for high-resolution PET applications *J. Nucl. Med.* **48** 115–21
Surti S, Karp J S, Perkins A E, Cardi C A, Daube-Witherspoon M E, Kuhn A and Muehllehner G 2005 Imaging performance of A-PET: a small animal PET camera *IEEE. Trans. Med. Imaging.* **24** 844–52
van Dam H T, Seifert S, Vinke R, Dendooven P, Löhner H, Beekman F J and Schaart D R 2011 A practical method for depth of interaction determination in monolithic scintillator PET detectors *Phys. Med. Biol.* **56** 4135–45
Wang Y, Seidel J, Tsui B M, Vaquero J J and Pomper M G 2006 Performance evaluation of the GE healthcare eXplore VISTA dual-ring small-animal PET scanner *J. Nucl. Med.* **47** 1891–900
Wienhard K, Dahlbom M, Eriksson L, Michel C, Bruckbauer T, Pietrzyk U and Heiss W D 1994 The ECAT EXACT HR: performance of a new high resolution positron scanner *J. Comput. Assist. Tomogr.* **18** 110–8
Yamaya T, Hagiwara N, Obi T, Tsuda T, Kitamura K, Hasegawa T, Haneishi H, Inadama N, Yoshida E and Murayama H 2006 Preliminary resolution performance of the prototype system for a 4-layer DOI-PET scanner: jPET-D4 *IEEE Trans. Nucl. Sci.* **53** 1123–8
Yamaya T, Mitsuhashi T, Matsumoto T, Inadama N, Nishikido F, Yoshida E, Murayama H, Kawai H, Suga M and Watanabe M 2011 A SiPM-based isotropic-3D PET detector X'tal cube with a three-dimensional array of 1 mm^3 crystals *Phys. Med. Biol.* **56** 6793–807
Yang Y, Dokhale P A, Silverman R W, Shah K S, McClish M A, Farrell R, Entine G and Cherry S R 2006 Depth of interaction resolution measurements for a high resolution PET detector using position sensitive avalanche photodiodes *Phys. Med. Biol.* **51** 2131–42
Yang Y, Wu Y, Qi J, James S S, Du H, Dokhale P A, Kanai S S, Farrell R and Cherry S R 2008 A prototype PET scanner with DOI-encoding detectors *J. Nucl. Med.* **49** 1132–40
Yoon H S, Ko G B, Kwon S I, Lee C M, Ito M, Song I C, Lee D S, Hong S J and Lee J S 2012 Initial results of simultaneous PET/MRI experiments with an MRI-compatible silicon photomultiplier PET scanner *J. Nucl. Med.* **53** 608–14